PHYSICAL REVIEW B VOLUME 40, NUMBER 15 15 NOVEMBER 1989-II

Kinetics of dopant incorporation using a low-energy antimony ion beam during growth of Si(100) films by molecular-beam epitaxy

W.-X. Ni, J. Knall, M. A. Hasan, G. V. Hansson, J.-E. Sundgren, and S. A. Barnett*
Department of Physics, Linköping University, S-581 83 Linköping, Sweden

L. C. Markert and J. E. Greene
Department of Materials Science, The Coordinated Science Laboratory, and The Materials Research Laboratory, University of Illinois, 1101 West Springfield Avenue, Urbana, Illinois 61801
(Received 17 May 1989)

n-type Si(100) films have been grown by molecular-beam epitaxy utilizing low-energy Sb ion-beam doping. The kinetics of dopant incorporation were investigated as a function of acceleration potential ($V_{Sb^+}=50-400$ V), deposition temperature ($T_s=550-1050\,^\circ$C), and Si growth rate ($R_{Si}=0.05-0.8$ nm s^{-1}). The Sb incorporation probability σ_{Sb^+} using accelerated-ion doping was up to 5 orders of magnitude higher than was obtainable with thermal Sb beams. In fact, σ_{Sb^+} was unity for $V_{Sb^+}\geq 300$ V at $T_s \leq 850\,^\circ$C. At lower acceleration potentials, σ_{Sb^+} was temperature and deposition-rate dependent. However, even at $V_{Sb^+}=50$ V and $T_s\geq 650\,^\circ$C, σ_{Sb^+} was still more than 1 order of magnitude higher than for thermal doping. Moreover, surface-segregation-induced profile broadening Δ_{Sb}, which for thermal-beam doping was ≥ 80 nm per concentration decade for $T_s \leq 650\,^\circ$C, was less than the depth resolution of the measurement, i.e., $\Delta_{Sb}\leq 12$ nm per concentration decade. The experimental incorporation results, $\sigma(V_{Sb^+},T_s,R_{Si})$, were found to be well described using a multisite model (including surface, bulk, and three intermediate sites) in which dopant surface segregation, incorporation, and bulk diffusion are accounted for by solving simultaneous transition-rate equations.

I. INTRODUCTION

Dopant incorporation behavior in single-layer as well as modulation-doped films grown by Si molecular-beam epitaxy (MBE) is of interest for both basic studies and device applications.[1,2] The most commonly used doping method during film growth by MBE is coevaporation from effusion cells. However, doping by coevaporation, while possessing the advantage of being technologically simple, has several severe limitations. Most of the dopants employed in Si technology, including P, As, Sb, Al, Ga, and In, exhibit low and exponentially-temperature-dependent incorporation probabilities σ. This not only limits maximum obtainable doping concentrations [C_{max} for In in Si(100), for example, is $\leq 5\times10^{15}$ cm^{-3} (Ref. 3)] but also requires extremely good control of both the temporal and spatial dependence of the substrate temperature during deposition. Furthermore, except at high growth temperatures, T_s, for which σ is low due to rapid dopant desorption, dopant surface segregation during MBE growth results in steady-state surface coverages Θ which can be substantial fractions of a monolayer (ML). This, in turn, gives rise to segregation-induced profile broadening Δ of up to several hundred nm per concentration decade. In the case of Sb, for example, $\Theta_{Sb}=1$ ML and $\Delta_{Sb}\geq 80$ nm per concentration decade have been reported.[4,5] Such high dopant coverages provide further restrictions on the maximum doping concentrations that can be obtained by coevaporation during MBE without introducing high defect concentrations which degrade electronic properties. For Sb, C_{max} is $\leq 10^{18}$ cm^{-3}.[5,6,7]

Doping techniques involving the use of accelerated ions have been developed to provide better control over dopant concentrations and depth distributions during Si MBE growth. For example, it has been shown that the incorporation probability of Sb,[8] As,[8] and In (Ref. 3) in Si can be increased by recoil implantation of surface-accumulated dopant species during growth. The ion bombardment is provided by applying a negative potential to the substrates in order to accelerate the ionized fraction of the electron-beam evaporated Si flux. However, since this method relies on dopant surface accumulation, significant profile broadening is still obtained unless a "build-up–flash-off" technique is employed in order to change the surface dopant coverage while interrupting the growth.[9] In addition, obtaining reasonable incorporation probabilities for Sb, as an example, requires Si acceleration of ~ 1000 V which has been shown to result in residual lattice damage.[10]

A more direct approach to increase dopant incorporation probabilities is to ionize and accelerate the dopant atoms themselves. Several groups have demonstrated orders of magnitude increases in σ with concomitant decreases in Δ for Sb,[11,12] As,[13] and In.[14] However, it has been shown that if the ion energy is too high, significant residual lattice damage degrades the electrical quality of as-deposited films.[13] On the other hand, in a recent

 ©1989 The American Physical Society

study, temperature-dependent Hall and resistivity measurements showed that 200 eV In^+ ions are incorporated, at concentrations up to and exceeding the equilibrium solid-solubility limits, into substitutional lattice sites with no evidence of residual lattice damage in MBE Si films grown at 800°C.[15] A unity incorporation probability σ_{In^+} was obtained for In^+ energies ≥ 200 V and $T_s < 900\,°C$.[14]

In this paper, we present the results of an investigation of the incorporation of Sb ions as a function of ion acceleration potential V_{Sb^+}, film growth temperature T_s, and film growth rate R_{Si}. The incorporation probability of thermal Sb, σ_{Sb^0}, ranged from ≈ 0.4 at $T_s = 575\,°C$, to 10^{-3} at 700 °C, to 10^{-5} at 800 °C. However, increases in σ_{Sb^+} by up to 5 orders of magnitude were obtained using accelerated-beam doping from an electron-impact single-grid low-energy ion source. In fact, the incorporation probability was unity with $V_{Sb^+} \geq 300$ V and $T_s \leq 850\,°C$, and abrupt doping profiles were obtained over a wide temperature range for $V_{Sb^+} \geq 200$ V. At lower acceleration potentials, σ_{Sb^+} was temperature dependent for $T_s \geq 600\,°C$. However, even at $V_{Sb^+} = 50$ V and $T_s \geq 650\,°C$, the incorporation probability was more than ten times higher than for thermal doping. The experimental results are explained using a multisite kinetic model (including surface, bulk, and three intermediate sites) in which dopant surface segregation, incorporation, and bulk diffusion are described in terms of trapping and site exchange. Calculated incorporation probabilities and segregation ratios were obtained by solving simultaneous transition-rate equations.

II. EXPERIMENTAL PROCEDURE

A. Antimony ion source

The low-energy Sb ion source used in this study consists of an effusion cell and a discharge chamber which are similar in design to earlier ion-doping sources.[16,17] The geometry of the orifice between the two chambers, as well as the ion optics, have been modified to be suitable for solid Sb (purity of 99.999%) in the form of crystallites. Antimony ions are generated by electron-impact in a discharge supported by Sb_4 vapor, without a carrier gas, and accelerated using a single multiaperture graphite grid. The beam divergence angle was approximately 20°. At source-to-substrate distances ≥ 25 cm, the ion current density was uniform to better than $\pm 15\%$ over an area of $\sim 5\ cm^2$. The Sb ionization efficiency varied between 3% and 35% depending on the discharge conditions. For some experiments, an electrostatic mirror deflector was installed above the source in order to obtain a beam free of neutral Sb species.

The source was mounted in a standard 11.43-cm-diam effusion-cell port in the MBE chamber. Ion current densities j_{Sb^+} measured by a translatable Faraday cup at the sample position ranged from 10^{-12} to $10^{-6}\ A\,cm^{-2}$ in these experiments. The ion current was controlled primarily by the discharge current but was also influenced by the effusion-cell temperature and the acceleration potential.

Since antimony evaporates primarily as Sb_4 molecules,[18] which are partially dissociated in the ion source discharge, the net flux of Sb atoms incident at the substrate surface cannot simply be deduced from the beam current. In order to analyze the extracted ion-beam flux, charge-to-mass ratio measurements were carried out in a separate vacuum chamber using the magnetic-field ion-optics system shown schematically in Fig. 1. After the antimony ions passed through a narrow slit (~ 0.8 mm) above the ion gun, they were electrostatically retarded to a kinetic energy of 12 eV and then deflected in a semicircle by the magnetic field. Using a translatable ion probe, it was found that the deflected beam was split into several components at different distances from the slit, as shown in Fig. 2. From the geometry of the mass-separation system and assuming that the antimony species from the source are singly ionized,[19] the expected positions for Sb_1^+, Sb_2^+, Sb_3^+, and Sb_4^+ ions were calculated and found to agree well with measured peak positions. Using the intensities under each peak, the weight factors are 0.43, 1.00 ≤ 0.02, and 0.43 for Sb_1^+, Sb_2^+, Sb_3^+, and Sb_4^+, respectively. These values are almost independent of the discharge currents and extraction voltages used in the present experiments. Hence, the ion-beam current can be converted to an antimony dopant flux by taking a weighted average of 2.2 for the number of atoms per ionized cluster.

B. Experimental details

All films studied were grown in a Vacuum Generators V-80 Si MBE system which has been described in detail previously.[17] The system base pressure was better than 10^{-10} Torr after baking for 24 h at 150 °C. During film growth, the pressure in the main chamber rose to $\sim 5\times10^{-9}$ Torr. The Si growth rate R_{Si} provided by a magnetically deflected electron-beam evaporator was, unless otherwise noted, maintained at $\sim 0.17\ nm\,s^{-1}$ ($8.5\times10^{14}\ cm^{-2}\,s^{-1}$) as monitored by

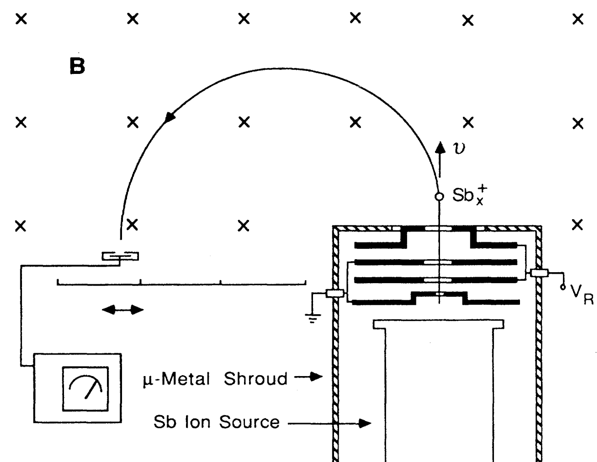

FIG. 1. Schematic drawing of the experimental arrangement used to determine the charge-to-mass ratio of accelerated ions. V_R is the retarding voltage.

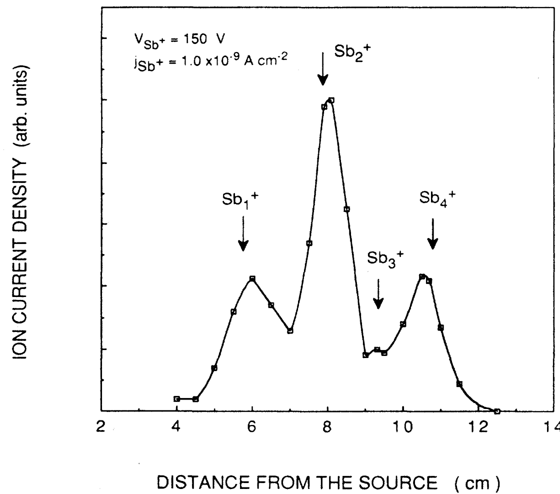

FIG. 2. Measured ion-current density vs distance from exit slit above the ion source. (See Fig. 1.) A magnetic field of 0.2 T and a retarding voltage of 138 V were used. The arrows show calculated positions for various ion species.

both a quartz-crystal monitor and a nude ionization gauge. Thicknesses of as-deposited films were measured using a microstylus profilometer.

The substrates used for most of the experiments were 1.0×2.5 cm^2 plates cut from boron-doped, mirror-polished, Si(100) wafers with room-temperature resistivities and hole concentrations of ~10 Ω cm, and 1×10^{15} cm^{-3}, respectively. Before insertion into the MBE chamber, the samples were first ultrasonically degreased in successive rinses of trichloroethane, acetone, ethanol, and deionized water, and then dipped in 2% dilute HF to remove the native oxide. This was followed by a two-step oxidation-etching procedure starting with the growth of an oxide in boiling NH_4OH:H_2O_2:H_2O (1:1:4). This oxide was then etched away in a 2% HF solution, and a final oxide with a thickness of ~1 nm was grown in boiling HCl:H_2O_2:H_2O (1:1:3). The samples were then loaded into a magazine which was transferred through a differentially pumped load-lock into the MBE growth chamber.

Immediately prior to Si film growth, the substrates were resistively heated in ultrahigh vacuum to ~550 °C for 5 min for out-gassing and then to ~900 °C for 2 min to desorb the thin protective silicon-oxide layer. This procedure generally resulted in clean surfaces exhibiting sharp 2×1 patterns by both low-energy and reflection high-energy electron diffraction (LEED and RHEED) with no evidence by Auger-electron spectroscopy (AES) of residual impurities. However, for a few substrates, minor carbon contamination was indicated by RHEED patterns, which exhibited two weak bulk-SiC diffraction spots in addition to the Si(100)2×1 pattern. The temperature of the substrates T_s during sample cleaning and film growth was monitored by an infrared pyrometer calibrated as described in Ref. 17.

Dopant profiles in as-deposited Si MBE films were measured by secondary-ion mass spectrometry (SIMS) using a Cameca IMS-3F microprobe system operated with a 17 keV, 1.25 μA, Cs^+ primary ion beam. A Sb-doped, 5×10^{17} cm^{-3}, bulk Si(100) sample, electrically characterized by Hall and resistivity measurements, and Sb-ion-implanted wafers were used as standards to convert SIMS profiles from intensities to Sb concentration units. Reported Sb doping levels are estimated to be accurate to within a factor of 2. The lowest detectable Sb concentration was approximately 10^{16} cm^{-3}.

III. EXPERIMENTAL RESULTS

A. Dopant profiles

Figure 3 shows a typical SIMS depth profile from an Sb ion-beam-doped multilayer structure grown at temperatures between 650 °C and 1050 °C. The layers were grown at successively lower temperatures in order to minimize the effects of bulk diffusion on previously grown layers during growth of subsequent layers. The approximately 120-nm-thick doped layers were separated by ~60-nm-thick undoped Si buffer layers. The doping was carried out with $V_{Sb^+}=300$ V and an ion flux $J_{Sb^+}=3.5\times10^{10}$ cm^{-2} s^{-1}. For a unity ion incorporation probability, this corresponds to a doping level of 2×10^{18} cm^{-3} as indicated in the figure by the dashed lines. The contribution to the doping profiles in Fig. 3 due to the flux of neutrals from the Sb ion source is negligible as discussed in Sec. III B. From Fig. 3, it can be seen that essentially all accelerated antimony ions were incorporated into the film for layers grown at $T_s\leq850$ °C.

The measured profile broadening Δ_{Sb} (defined as the

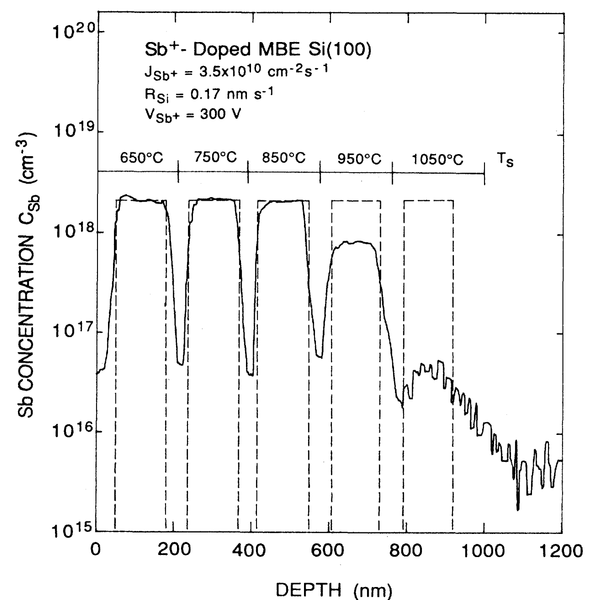

FIG. 3. Antimony concentration depth profile obtained by SIMS from a Si(100) MBE film containing layers doped with a 300 V accelerated Sb ion beam at different growth temperatures. The dashed curve shows the ideal profile ($\sigma_{Sb^+}=1$) for the corresponding Sb^+ flux and Si rate.

profile width per decade change in dopant concentration) is ~ 12 nm per decade for layers grown at $T_s \leq 900\,°C$. The intrinsic profile broadening in ion-doped layers is actually ≤ 12 nm per decade since the observed Δ values were limited by SIMS measurements artifacts such as ion mixing and surface roughening introduced by sputtering. As a comparison, the measured profile broadening for samples doped using a thermally evaporated Sb beam is two to five times larger ($\Delta_{Sb^0} \approx 30-80$ nm per decade) for growth temperatures between 500 °C and 675 °C.

The sharp profiles obtained for the ion-doped samples indicate that the excessive dopant surface segregation and accumulation which occurs during thermal doping is significantly suppressed in the ion-beam doping process. However, at higher growth temperatures, even the ion-doped profiles begin to broaden due to bulk diffusion during growth. For example, at $T_s = 1050\,°C$, the profiles become very smeared out with $\Delta_{Sb} > 180$ nm. In addition to the substrate temperature, the shape of the doping profile also depends on the ion energy and film growth rate. For the lowest ion acceleration potential investigated (50 V), there is a slight increase in the profile broadening compared to the 300 V data shown in Fig. 3. However, Δ_{Sb^+} is still much smaller than for thermal doping.

Complete antimony incorporation and very low dopant surface segregation combined with an accurately controlled ion-beam current provide the ability to obtain virtually any desired doping profile shape. Figure 4 shows, as an example, a modulation-doped profile with a sawtooth shape. This profile was achieved by decreasing the current density of a $V_{Sb^+} = 300$ V beam from 6.0×10^{-9} to 6.0×10^{-12} A cm^{-2} ($J_{Sb^+} = 4 \times 10^{10} - 4 \times 10^{7}$ cm^{-2} s^{-1}). The ion current was, in this case, controlled by regulating the discharge current. The arrow in Fig. 4 indicates the SIMS detection limit.

B. Incorporation probability of Sb ions

The incorporation probability of accelerated antimony ions in Si(100) during MBE film growth is determined from experimental parameters by

$$\sigma_{Sb^+} = C_{Sb} R_{Si} / J_{Sb^+} , \quad (1)$$

where the steady-state Sb doping concentration C_{Sb} is obtained from SIMS data, J_{Sb^+} is the ion-doping flux, and R_{Si} is the Si growth rate. For the growth conditions used in these experiments, σ_{Sb^0}, the incorporation probability of thermal antimony is much less than σ_{Sb^+}, as demonstrated below. Thus, the flux of thermal species can be neglected.

Figure 5 shows σ_{Sb^+} values, obtained from profiles such as the one given in Fig. 3 versus film growth temperature T_s for ion acceleration potentials V_{Sb^+} between 50 and 400 V. The dotted lines correspond to calculated curves based upon the incorporation model presented in Sec. IV. σ_{Sb^0} values are also given in Fig. 5 and shown to range from 1 to several orders of magnitude smaller than σ_{Sb^+}, even with the lowest acceleration potential, $V_{Sb^+} = 50$ V, for $T_s \geq 650\,°C$. Thus the neutral antimony species emitted from the ion source have negligible effect on measured ion incorporation probabilities in the present experiments except at $T_s \leq 575\,°C$. σ_{Sb^+} is essen-

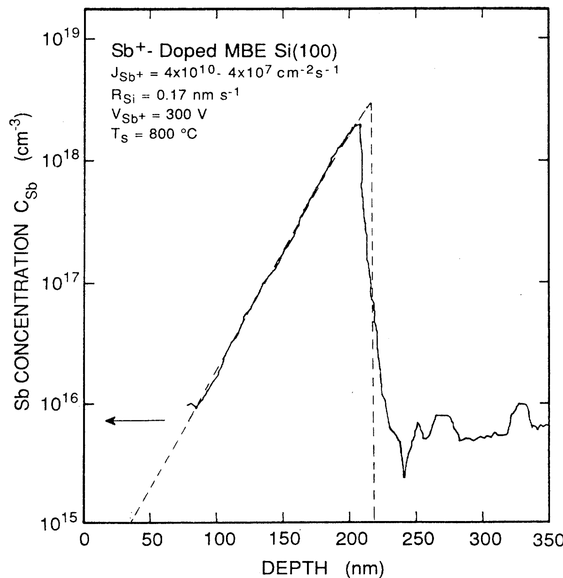

FIG. 4. Antimony modulation doping profile achieved by changing the 300 V accelerated Sb ion-beam flux from 4×10^{10} cm^{-2} s^{-1} to 4×10^{7} cm^{-2} s^{-1} during MBE Si(100) growth at $T_s = 800\,°C$. The dashed line shows the shape of the intended profile and the arrow indicates the SIMS detection limit.

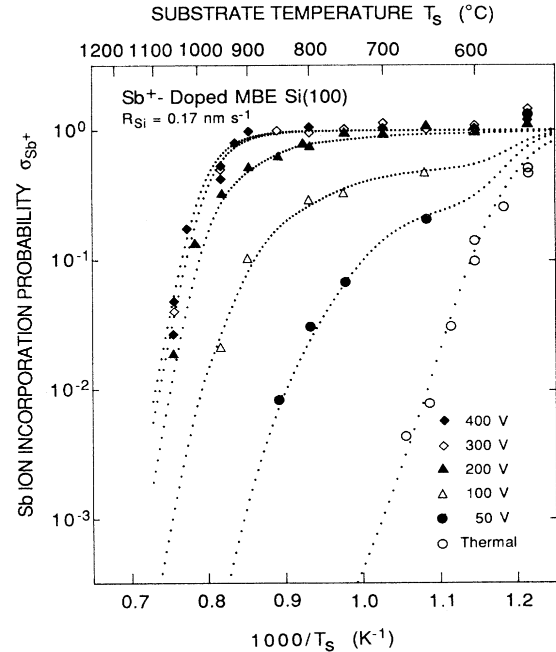

FIG. 5. Sb incorporation probability σ_{Sb^+} as a function of ion acceleration potential V_{Sb^+} and MBE Si(100) growth temperature T_s. The dotted curves show fitted results using the model described in Sec. IV B.

tially unity for $V_{\mathrm{Sb}^+} \geq 300$ V and growth temperatures up to $\approx 850\,^\circ\mathrm{C}$ but decreases rapidly at higher temperature. For film grown with $B_{\mathrm{Sb}^+} \leq 200$ V, σ_{Sb^+} varies with T_s at all growth temperatures investigated and does not reach unity even at $T_s = 650\,^\circ\mathrm{C}$.

The mechanism of accelerated-ion incorporation/p during Si MBE was further probed by varying the film growth rate R_{Si} between 0.05 and 0.8 $\mathrm{nm\,s^{-1}}$ [$(0.25-4)\times 10^{15}\ \mathrm{cm^{-2}\,s^{-1}}$] at constant deposition temperature with $V_{\mathrm{Sb}^+} = 100-300$ V. Results for $T_s = 900\,^\circ\mathrm{C}$ are summarized in Fig. 6. With $V_{\mathrm{Sb}^+} = 100$ V, σ_{Sb^+} increased in a smooth continuous manner with increasing R_{Si}. This is reminiscent of previous studies carried out with thermal Sb in which σ_{Sb} was found to be proportional to R_{Si}.[5] However, the data in Fig. 6 show quite different behavior with $V_{\mathrm{Sb}^+} = 200$ and 300 V, for which σ_{Sb^+} initially increases rapidly with R_{Si} while at higher growth rates the increase becomes much more gradual. For $R_{\mathrm{Si}} > 0.15\ \mathrm{nm\,s^{-1}}$ ($7.5\times 10^{14}\ \mathrm{cm^{-2}\,s^{-1}}$), σ_{Sb^+} was near unity with $V_{\mathrm{Sb}^+} = 300$ V.

The steady-state incorporated dopant concentration C_{Sb} was also investigated as a function of the incident Sb ion flux, J_{Sb^+}. Typical results in which C_{Sb} varies linearly with J_{Sb^+} are shown in Fig. 7 for $V_{\mathrm{Sb}^+} = 150$ V and $T_s = 800\,^\circ\mathrm{C}$. This implies, first of all, that the results shown in Figs. 5 and 6 (i.e., σ_{Sb^+} versus T_s and R_{Si}) are independent of J_{Sb^+}. Second, the linear relationship between C_{Sb} and J_{Sb^+} indicates that the incorporation of Sb ions during Si MBE growth follows first-order kinetics up to at least $C_{\mathrm{Sb}} \approx 2\times 10^{19}\ \mathrm{cm^{-3}}$, the highest concentration investigated.

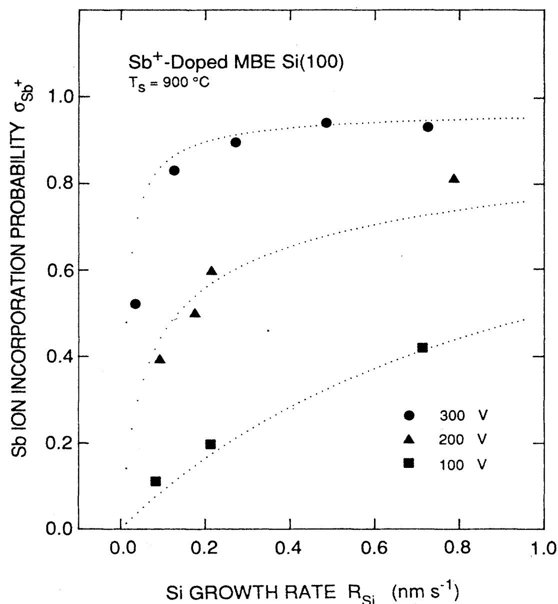

FIG. 6. Sb incorporation probability σ_{Sb^+} as a function of ion acceleration potential V_{Sb^+} and the MBE Si(100) growth rate R_{Si}. The dotted curves show calculated results using the model in Sec. IV.

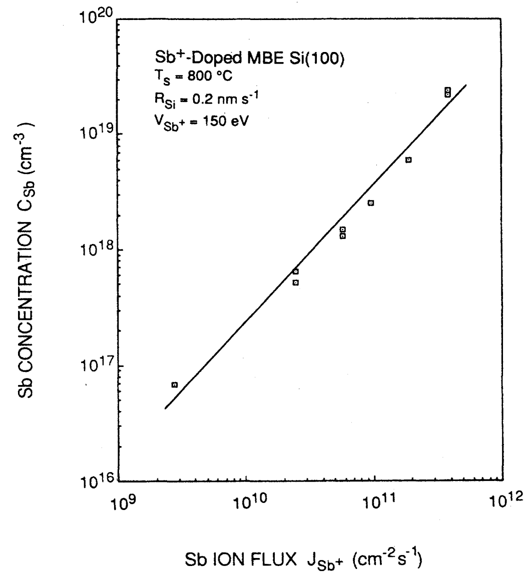

FIG. 7. Antimony concentration incorporated in MBE Si(100) films vs incident Sb ion flux at a growth temperature $T_s = 800\,^\circ\mathrm{C}$ and an ion acceleration potential $V_{\mathrm{Sb}^+} = 150$ V. The film growth rate was $R_{\mathrm{Si}} = 0.2\ \mathrm{nm\ s^{-1}}$.

IV. DISCUSSION

A. Incorporation of Sb ions during Si MBE

Coevaporative doping using a thermal Sb dopant beam, provided by a standard effusion cell, during Si MBE results in low incorporation probabilities, σ_{Sb^0}, and smeared doping profiles. The latter is caused by extensive accumulation of Sb atoms on the Si surface at typical film growth temperatures. This dopant accumulation layer gives rise to continued Sb incorporation even after shuttering off the dopant beam flux during, for example, the growth of a subsequent buffer layer. Moreover, loss of dopant atoms by desorption from the surface accumulation layer leads to an exponential decrease in σ_{Sb^0} with increasing T_s.

The present experimental results show that the use of low-energy ion doping completely alters the kinetics of dopant incorporation. For $V_{\mathrm{Sb}^+} = 50-400$ V, the projected range r_p of implanted Sb ions in Si and the relative straggle $\Delta r_p / r_p$ are estimated from an extrapolation of high-energy implantation data[20] to be 0.1–1.1 nm and ≈ 0.3, respectively. Thus, for $V_{\mathrm{Sb}^+} \geq 200$ V, most of the ions end up in bulklike lattice sites and become trapped in the Si film unless the substrate temperature is sufficiently high ($\geq 850\,^\circ\mathrm{C}$) to allow significant diffusion to the surface and subsequent desorption. The rate-limiting kinetic barrier for Sb becomes the activation energy E_b for bulk diffusion 3.65 eV,[21] since the Sb desorption energy from Si(100) is only 2.40 eV.[18] This interpretation is supported by recent experiments on In ion-beam adsorption-desorption rates,[3] where temperature-programmed desorption (TPD) spectra showed that trapped 400 eV In ions desorbed with a higher activation

energy than In atoms from surface adlayers. In the latter case, a surface binding energy of 2.85 eV was found, whereas in the former case an apparent activation energy of 3.5 eV ($\sim E_b$) (Ref. 22) was obtained, assuming the same frequency factor. A similar effect was also observed for desorption of Sb atoms recoil implanted by 2-keV Ar^+ ion bombardment of Sb monolayers on Si(100).[23]

In situ AES analyses were used in an attempt to estimate steady-state Sb surface coverages Θ_{Sb} during film growth at 750 °C with $V_{Sb^+} \geq 200$ V, J_{Sb^+} values chosen to yield $C_{Sb} \geq 10^{18}$ cm^{-3}, and an electrostatic mirror deflector in front of the ion source to provide a dopant beam free of neutral Sb species. The results showed that Θ_{Sb} was smaller than the detection limit, i.e., <0.01 ML. Hence, dopant surface accumulation was significantly suppressed compared to Θ_{Sb} values (>0.1 ML) observed with thermal doping sources operated under conditions yielding the same bulk Sb concentrations. As discussed below, this can be understood based upon a model in which the accelerated dopant species were trapped by high-energy barriers within the lattice and retained long enough to be embedded by subsequently deposited Si layers. The resulting decrease in Sb surface segregation gives rise to a corresponding decrease in the dopant desorption rate and thus an increase in the dopant incorporation probability. σ_{Sb} is no longer a function of Θ_{Sb} and dopant concentrations exceeding the equilibrium solid-solubility limit, as has been observed for In^+ ion doping during Si MBE,[15] are possible.

For ion acceleration potentials ≤ 200 V, σ_{Sb^+} is less than unity at growth temperatures above 650 °C and does not vary with T_s according to a simple exponential decay corresponding to surface desorption as in the case of thermal-beam doping. This suggests that at these very low acceleration energies, dopant loss occurs by desorption from several different higher binding energies. The Si(100)2×1 surface is relatively open and the upper bilayer is not atomically smooth during growth allowing near-surface sites with different coordination to be accessed by low-energy ions. The distribution of trapping sites is enlarged in the present experiments since the ion beam is composed of different size Sb clusters $Sb_x{}^+$ ($x=1,2,4$) with energies per impinging atom of (eV_{Sb^+}/x).

From the above discussion, the influence of R_{Si} on σ_{Sb^+}, especially apparent at either high T_s or low V_{Sb^+}, can be understood. For example, at high growth temperatures (e.g., $T_s \geq 850$ °C for $R_{Si} \approx 0.1$ nm s^{-1}), the Sb bulk diffusion rate is comparable to the Si growth rate, and hence, for very shallow ion ranges, some dopant atoms are able to diffuse back to the surface where they desorb before being buried by subsequently deposited Si layers. However, the percentage of Sb atoms returning to the growth surface decreases as the film growth rate is increased, resulting in higher σ_{Sb^+} values. For given T_s and R_{Si} values, σ_{Sb^+} also increases with increasing V_{Sb^+}, since the fraction of trapped dopant atoms segregating back to the growth surface decreases as the dopant atoms penetrate deeper into the bulk.

Samples grown at $T_s = 800$ °C with $V_{Sb^+} = 150$ V were examined by temperature-dependent Hall measurements in conjunction with both cross-sectional and plan-view transmission electron microscopy (XTEM and TEM).[12] The samples exhibited 100% electrical activation over the entire concentration range examined, $5\times10^{16}-2\times10^{19}$ cm^{-3}, with carrier mobilities equal to bulk values. XTEM and TEM examinations showed no precipitates or other extended defects. Thus, based upon both electrical and TEM studies, there was no evidence of residual lattice damage introduced by the antimony ion beam.

B. Kinetic model for incorporation of accelerated Sb ions

In this section, a kinetic model, based upon the results discussed above, is proposed to quantitatively describe accelerated low-energy ion incorporation during Si MBE growth. The model is then used in the next section to describe the experimental data.

Following work on surface segregation[24,25] and the incorporation of thermally evaporated Sn during GaAs MBE growth,[26] the present model is based on an exchange process for dopant atoms moving between potential wells corresponding to lattice sites in the near-surface region. The dynamical situation involving simultaneous Si growth and ion doping is taken into account.

As is known from observations of RHEED intensity oscillations, Si MBE growth proceeds via quasi-two-dimensional layer-by-layer deposition.[27] The growth surface for Si(100) forms a 90°-rotated two-domain 2×1 reconstruction which can be described using the buckled dimer model.[28] Figure 8(a) shows the 2×1 reconstructed Si(100) surface, viewed in the $[01\bar{1}]$ direction with substitutional Sb atoms randomly distributed in the near-surface region. It should be noted that the actual situation is surely more complicated due to the existence of steps, surface defects, etc., which lead to additional sites. However, as a first approximation, the model calculations are based upon ideal Si(2×1) surfaces with sites in near-surface layers labeled as shown in Fig. 8(a). Layer 1 corresponds to threefold coordinated dimer atoms. Atoms in layers 2 and 3, while exhibiting fourfold coordination, are shifted significantly from bulk positions.[29] Even layer 4 can, according to theoretical studies of the atomic structure of the Si(100)2×1 reconstruction, be affected by surface strain.[30] Starting from layer 5, the dopant atoms are assumed to be positioned in completely bulk-like sites.

Figure 8(b) shows a schematic potential-energy diagram, used to describe the exchange processes discussed below, in which each minimum corresponds to a successively deeper Si lattice site. The minima are separated by a distance of approximately $a_0/4$ along the [100] direction, where a_0 is the lattice constant of Si. We initially attempted to model incorporation kinetics by assuming that only two or three layers are different from the bulk, but found it necessary to use four layers in order to fit the experimental data. The potential-energy barriers for passage between layers in the near-surface region are assumed to be smaller than the bulk diffusion barrier. En-

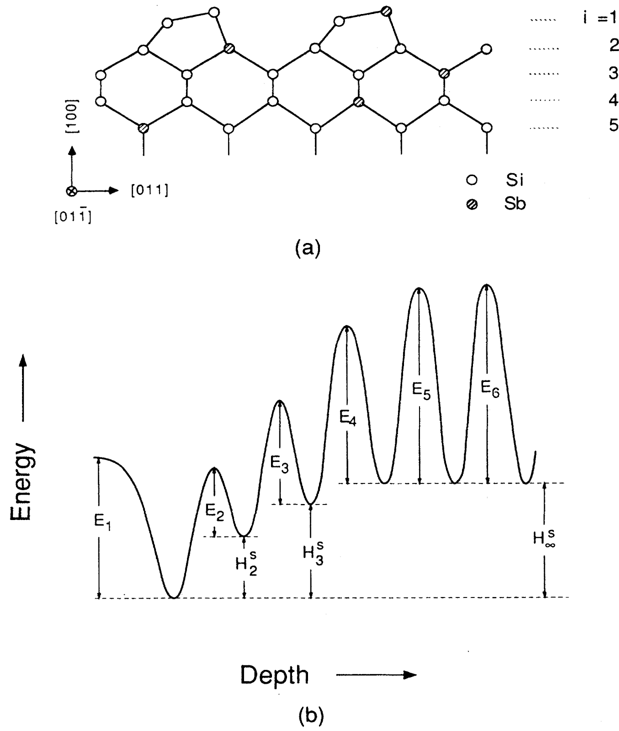

FIG. 8. (a) The reconstructed Si(100)2×1 near-surface region, viewed in the [01$\bar{1}$] direction, with randomly distributed Sb dopant atoms. (b) Schematic diagram representing energy levels of substitutional sites in the first six layers. E_i $(i=1,2,\ldots,6)$ are activation barriers while H_j^s $(j=2,\ldots,\infty)$ are Gibbs enthalpies.

ergy differences between a bulk site and sites in these first four layers are due to the enthalpy H^s of dopant surface segregation.

The model describes both thermally evaporated and accelerated Sb doping in a coherent way. The major difference between these techniques is the average "penetration depth" of the dopant into the lattice. To simplify the calculations, a one-dimensional model is used in which near-surface exchange processes are only allowed to occur between adjacent layers. From mass-balance considerations in conjunction with the experimental finding that Sb ion incorporation during Si MBE growth is a first-order process, the transition rates of dopant atoms in layers i are given by the following set of first-order time-dependent differential equations,

$$dn_1/dt=J_{d,1}-J_{\rm des}-J_{1,2}+J_{2,1}-F_{1,2}\ , \tag{2a}$$

$$dn_2/dt=J_{d,2}+J_{1,2}-J_{2,1}+J_{3,2}-J_{2,3}+F_{1,2}-F_{2,3}\ , \tag{2b}$$

$$dn_i/dt=J_{d,i}+J_{i-1,i}-J_{i,i-1}+J_{i+1,i}-J_{i,i+1}+F_{i-1,i}-F_{i,i+1}\ , \tag{2c}$$

$$dn_m/dt=J_{d,m}+J_{m-1,m}-J_{m,m-1}+F_{m-1,m}-F_{m,m+1}\ . \tag{2d}$$

The indices $i=1,2,\ldots,m$ in Eqs. (2a)–(2d) indicate successive layers from the surface and n_i is the number of dopant atoms per cm^2 in atomic layer i. For $i>m$, the calculations were truncated by setting $J_{m+1,m}=J_{m,m+1}$. $J_{\rm des}$ is the dopant desorption flux and $J_{i,j}$ is the dopant exchange flux (atoms cm^{-2} s^{-1}) between site i and the adjacent sites $j=i\pm1$. $F_{i,i+1}$ in Eq. (2) is an additional flux accounting for Si growth, and $J_{d,i}$ in Eq. (2) is the incident dopant flux to state i.

For a first-order process, $J_{\rm des}$ and $J_{i,j}$ can be written as

$$J_{\rm des}=K_{\rm des}n_1=n_1\nu_1\exp(-E_1/k_BT_s) \tag{3a}$$

and

$$J_{i,j}=r_{i,j}n_i=n_i\nu_i\exp[-(E_j+\Delta H_j^s)/k_BT_s] \quad (j=i+1,\ i\geq1)$$
$$=n_i\nu_i\exp(-E_i/k_BT_s) \quad (j=i-1,\ i\geq2)\ , \tag{3b}$$

where $K_{\rm des}$ and $r_{i,j}$ are the desorption and exchange coefficients, respectively. E_i is the energy barrier height and ν_i is the vibration frequency of atoms in site i. ΔH_i^s is the difference between enthalpies corresponding to state $i-1$ and state i. Furthermore, $F_{i,i+1}$ can be described by a term corresponding to dopant atoms continuously jumping from site i to site $i+1$ with a time constant $\tau(a_0/4)R_{\rm Si}$, i.e.,

$$F_{i,i+1}=n_i/\tau=4R_{\rm Si}n_i/a_0\ . \tag{4}$$

The sum over $J_{d,i}$, the incident dopant flux to state i, is equal to the total measured incident dopant flux,

$$J_d=\sum_{i=1}^{m}J_{d,i}\ . \tag{5}$$

The depth dependence of $J_{d,i}$ for an accelerated ion beam can be approximated using a discrete Gaussian function,

$$J_{d,i}=J_d\frac{\exp[-(\{i-1-[r_p/(a_0/4)]\}/[\Delta r_p/(a_0/4)])^2/2]}{\sum_{i=1}^{m}\exp[-(\{i-1-[r_p/(a_0/4)]\}/[\Delta r_p/(a_0/4)])^2/2]}\ , \tag{6}$$

where r_p and Δr_p are the projected range and the straggle, respectively.

Inserting Eqs. (3) and (4) into Eqs. (2a) and (2b) yields

$$dn_1/dt = J_{d,1} - (K_{des} + r_{1,2} + 1/\tau)n_1 + r_{2,1}n_2 , \quad (7a)$$

$$dn_i/dt = J_{d,i} + (r_{i-1,i} + 1/\tau)n_{i-1} - (r_{i,i-1} + r_{i,i+1} + 1/\tau)n_i + r_{i+1,i}n_{i+1} , \quad (7b)$$

$$dn_m/dt = J_{d,m} + (r_{m-1,m} + 1/\tau)n_{m-1} - (r_{m,m-1} + 1/\tau)n_m . \quad (7c)$$

The time-dependent dopant concentration in atomic layer i can then be calculated by numerically integrating Eqs. (7a)–(7c) using a four-order Runge-Kutta method[31] with the initial conditions $n_i(t=0)=0$ for $i=1,2,\ldots,m$. In computing steady-state profiles, the program stops when the densities of dopant atoms in each of the deepest three states are equal to within 10^{-3}. The steady-state incorporation probability can then be computed from the expression

$$\sigma = n_m/(J_d\tau) . \quad (8)$$

The segregation ratio r can also be straightforwardly defined as

$$r = n_1/n_m . \quad (9)$$

C. Comparison of model calculations with experimental results

Model calculations were carried out for both thermal-Sb and accelerated-Sb^+ doping. Sb/Si(100) surface desorption and bulk diffusion activation energies were taken from experimental results found in the literature. Barnett *et al.*[18] have determined E_{des} and ν_s to be 2.40 eV and 2×10^{10} s^{-1}, respectively. For bulk diffusion, E_b is 3.65 eV and the preexponential diffusivity factor D_0 is 0.214 $cm^2 s^{-1}$ (Ref. 20) for doping levels $N_{Sb} \le 10^{19}$ cm^{-3}. D_0 can be converted to the frequecy factor ν_b by division with $(a_0/4)^2$ giving $\nu_b = 1.16\times10^{15}$ s^{-1}. In order to reduce the number of fitting parameters, the frequency factors for exchanges between the sites closest to the surface (i or $j=1,2,3$) were chosen equal to ν_s while for exchanges involving bulklike states ($i,j \ge 4$), the frequency factor was set equal to ν_b. The projected range r_p and the straggle Δr_p were extrapolated from high-energy implantation data.[20]

The Sb ion beam used in these experiments is composed of three primary ion species Sb_x^+ ($x=1,2,4$), which were accelerated to energies $E_{Sb_x} = eV_{Sb^+}/x$ per Sb atom. Thus, the incident ion profile cannot be described by a single Gaussian distribution. Instead, the weighted summation of all profiles $J_{d,i,x}$ with energy corresponding to eV_{Sb^+}/x is used, i.e.,

$$J_{d,i} = \sum_{x=1,2,4} J_{d,i,x} x A_x \Big/ \left[\sum_{x=1,2,4} x A_x \right] , \quad (10)$$

where A_x is the measured weighting factor for each constituent in the Sb_x^+ beam.

The energy values E_i and H_i^s for the intermediate states ($i=2,3,4$) are unknown. However, in the calculations described here, we have assumed that H_i^s decreases exponentially towards the surface with a length scale L corresponding to one atomic layer,

$$H_i^s = H_\infty^s (1 - \exp\{-[(i-1)a_0/4]/L\}), \quad i=1,2,3,4 . \quad (11)$$

Finally, the remaining four parameters, E_i ($i=2,3,4$) and H_∞^s, were used as fitting parameters.

The first 12 layers from the surface to the bulk were included in the program to ensure that the calculations converged to a steady-state condition. In order to determine the values of E_i ($i=2,3,4$) and H_∞^s, the model calculations were initiated by fitting measured data for $\sigma_{Sb^+}(V_{Sb^+}, T_s)$. The fitting procedure was first carried out for the thermal doping case in which the upper two sites dominate and the others have only a small influence. Since the surface desorption energy is known, only E_2 and H_∞^s are needed in this case.

The energy barriers associated with the deeper sites were determined by fitting data obtained using ions with increasing acceleration energy. After fitting the highest-energy data, the calculational procedure was reiterated for a fine adjustment. The values of E_i ($i=2,3,4$) and H_∞^s obtained, together with the other parameters used for the calculations of dopant incorporation probabilities versus V_{Sb^+} and T_s, are summarized in Table I. The value of H_∞^s obtained agrees with that obtained by Barnett and Greene[32] in modeling Sb incorporation in Si(111). The uncertainty in the reported parameters (E_i and H_∞^s) is approximately ±0.1 eV. A primary source of error is in the input parameters r_p and Δr_p.

The calculated values of σ_{Sb^+} versus V_{Sb^+} and T_s, obtained by using the parameters given in Table I, are shown as dotted curves in Fig. 5. The fitting procedure was also carried out using fewer near-surface layers. Figure 9 shows experimental data for σ_{Sb^+} versus $1/T_s$ with

TABLE I. Energy and vibration frequency parameters for sites used in the model calculations.

	1	2	3	4	≥ 5
E_i (eV)[a]	2.4	1.3	2.15	3.35	3.65
ΔH_i^s (eV)[b]		0.8	0.3	0.1	
ν_i (s^{-1})	2.0×10^{10}	2.0×10^{10}	2.0×10^{10}	1.16×10^{15}	1.16×10^{15}

[a] E_2, E_3, and E_4 are obtained by fitting experimental data.

[b] ΔH_i^s values are calculated from Eq. (11), where $H_\infty^s = 1.2$ eV is obtained by fitting experimental data.

$V_{Sb^+}=100$ V together with model calculations (best fits) based upon 1, 2, and 3 intermediate sites. As can be seen, five sites with different energies are required to obtain a good fit. For a lower number of sites, the calculated curves always contain clear break points rather than a gradual decrease in $\sigma_{Sb^+}(T_s)$.

In order to provide a further test of the model, the same set of parameter values was also used to calculate the rate-dependent incorporation probability for different ion acceleration potentials at constant T_s values. Excellent agreement with experimental results was obtained as shown in Fig. 6. The fact that the same parameter values could be used to fit both $\sigma(V_{Sb}, T_s)$ and $\sigma(V_{Sb}, R_{Si})$ supports the validity of our model.

Finally, Fig. 10 shows calculated values of the segregation ratio $r=n_1/n_m$ versus T_s and V_{Sb^+}. For thermal Sb doping ($V_{Sb^+}=0$) and growth temperatures above 500 °C, r first increases exponentially with T_s, reaches a maximum at $T_s \approx 820$ °C, and then decreases exponentially at higher temperatures. In the latter region, the dopant diffusion rate is larger than the film growth rate and equilibrium segregation is a reasonable approximation. This implies that r decreases with a slope determined by H^s_∞, which is 1.2 eV in the present case. For T_s near 820 °C, the diffusion rate is of the same order as the growth rate and equilibrium segregation is no longer valid. In this temperature range, the segregation rate begins to be kinetically limited. At growth temperatures less than 820 °C, r increases with increasing T_s even though the adatom desorption rate is also increasing exponentially with T_s. This occurs because the segregation ratio in the thermal-case does not depend on the desorption rate, but it is determined by the growth rate and the exponentially increasing segregation flux of dopant atoms across the E_2 potential barrier.

The transition temperature T^* between the equilibrium and the kinetically limited regime is ~820 °C in the present calculation, which is higher than the 720 °C value obtained previously by Barnett and Greene[32] for Sb/Si(111). Note that T^* in both calculations is strongly dependent on kinetic parameters such as the film growth rate and the adatom mobility in the near-surface region. The height of the E_2 barrier, in particular, strongly affects T^*. For example, if E_2 in the present case is reduced from 1.3 to 0.9 eV, T^* decreases from 820 °C to 750 °C. The latter value is, however, not consistent with our experimental incorporation data.

For accelerated-ion doping, the situation is quite different from that described above for thermal doping. Figure 10 shows calculated $r(T_s)$ results for Si(100) films grown at $R_{Si}=0.17$ nm s^{-1} and acceleration potentials $V_{Sb^+}=25$, 50, 100, 200, and 300 V. The segregation ratio

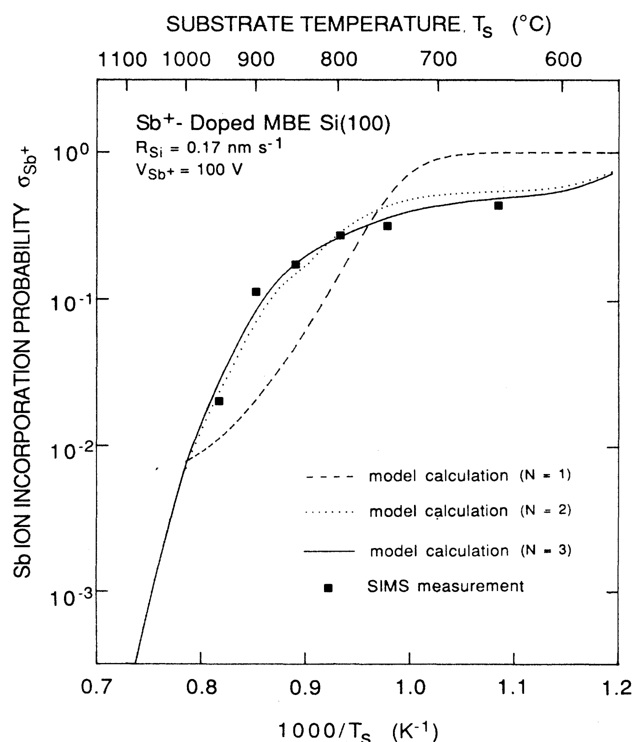

FIG. 9. Calculated Sb incorporation probabilities in Si(100) films grown by MBE as a function of substrate temperature T_s for a growth rate $R_{Si}=0.17$ nm s^{-1} and a Sb ion acceleration potential $V_{Sb^+}=100$ V. The calculations were carried out in the model discussed in Sec. IV with $N=1$, 2, or 3 intermediate sites between surface and bulk sites. The solid squares are measured data.

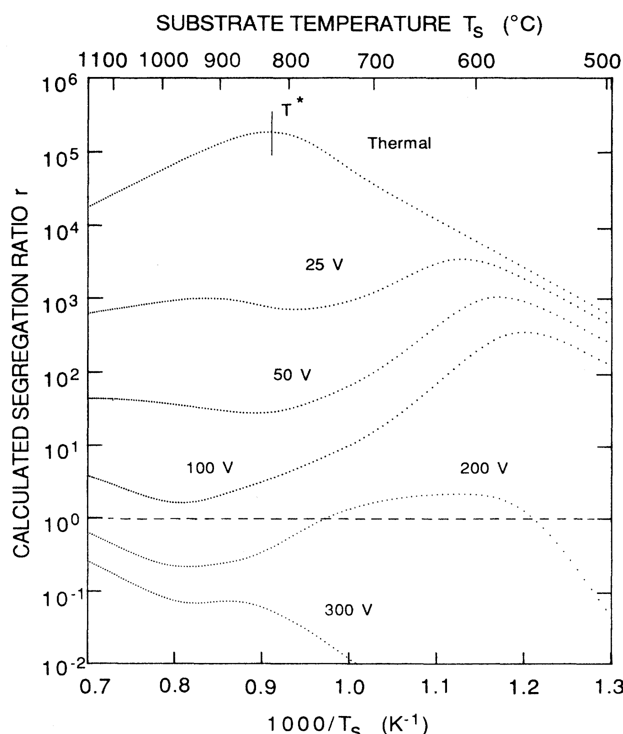

FIG. 10. Calculated segregation ratio r_1/r_m as a function of growth temperature T_s for different Sb ion acceleration potentials V_{Sb^+}.

decreases with increasing V_{Sb^+} as an increasing fraction of the dopant flux becomes trapped in sites with higher activation energies. This would be expected, in general, to result in higher-T^* values. In fact, the calculations show that equilibrium segregation is not achieved over the temperature range shown in Fig. 10.

As T_s is increased from the low-temperature side of the graph in Fig. 10, r first reaches a local maximum for accelerated-ion doping, E_x $(x \geq 3)$ values are larger than E_1, and desorption is thus a more important term than for the thermal doping case where $E_2 < E_1$. This gives rise to large effects at temperatures near 800 °C as r decreases by several orders of magnitude. With further increases in T_s more dopant species in near-surface trap sites move toward the surface, and $r(T_s)$ increases again toward thermal doping values. However, our results indicate that equilibrium segregation behavior is not achieved even at the highest growth temperatures used, 1200 °C, although the $V_{Sb^+}=25$ and 50 V curves do begin to turn over at $T_s \geq 920$ and 1150 °C, respectively. For $V_{Sb^+}=200$ V, r is near unity over most of the growth temperature ranges, but at higher acceleration potentials, $r \ll 1$ at low temperatures.

From the above results, we conclude that the strong-Sb surface-segregation effects observed during Si film growth with thermal doping can be avoided for a wide range of film growth temperatures through the use of an accelerated dopant beam with $V_{Sb^+} \geq 200$ V. Preliminary calculations of dopant depth distributions using the present incorporation model show that abrupt dopant profiles can be obtained with broadenings $\Delta_{Sb^+} \leq 6$ nm.

V. SUMMARY

Sb-doped Si films with doping concentrations between 5×10^{16} and 2×10^{19} cm^{-3} were grown by molecular-beam epitaxy utilizing a single-grid, low-energy Sb ion source. A detailed study of accelerated antimony ion incorporation showed that the low-energy ion source is capable of providing well-controlled doping profiles with a high, nearly temperature-independent, incorporation probability ($\sigma_{Sb^+} \approx 1$) and very little dopant-segregation-induced profile broading ($\Delta_{Sb} \leq 12$ nm) over a wide range of growth temperatures ($T \leq 850$ °C, for $V_{Sb^+} > 200$ V). An incorporation model including both kinetic and thermodynamic components has been proposed to explain the results. From a comparison of experimental data and model calculations, we conclude that the increase in σ_{Sb^+} is due to trapping of the implanted Sb ions in near-surface sites resulting in strongly attenuated, kinetically limited surface segregation during growth, lower dopant surface accumulation, and hence less dopant loss by desorption. To describe the temperature dependence of incorporation for very shallow implantation ($V_{Sb^+} < 200$ V), it is necessary to account for at least three intermediate sites between the surface and bulk sites. Activation energies associated with these intermediate sites were obtained by fitting experimental incorporation data.

ACKNOWLEDGMENTS

The authors are indebted to J. Jacobsson and K. Larsson for technical assistance during construction of the ion source. The work was financially supported by the Swedish Natural Science Research Council (NFR), the Joint Services Electronics Program, the Semiconductor Research Corporation, and the NASA Space Vacuum Epitaxy Center.

---

*Permanent address: Department of Materials Science and Engineering and The Materials Research Center, Northwestern University, Evanston, IL 60298-9990.

[1]J. C. Bean, in *Impurity Doping Processes in Silicon,* edited by F. F. Y. Wang (North-Holland, Amsterdam, 1981), p. 175.

[2]S. S. Iyer, in *Epitaxial Silicon Technology,* edited by B. J. Baliga (Academic, Orlando, 1986), p. 91.

[3]J. Knall, M.-A. Hasan, J.-E. Sundgren, A. Rockett, L. C. Markert, and J. E. Greene, in *Silicon Molecular Beam Epitaxy 2,* edited by J. C. Bean and L. J. Schowalter (Electrochemical Society, Pennington, New Jersey, 1988), p. 470.

[4]J. C. Bean, Appl. Phys. Lett. **33**, 654 (1978).

[5]R. A. Metzger and F. G. Allen, J. Appl. Phys. **55**, 931 (1984).

[6]U. König, E. Kasper, and H. J. Herzog, J. Cryst. Growth **52**, 151 (1981).

[7]F. A. d'Avitaya, S. Delage, and E. Rosencher, Surf. Sci. **168**, 483 (1986).

[8]R. A. A. Kubiak, W. Y. Leong, and E. H. C. Parker, Appl. Phys. Lett. **46**, 565 (1985).

[9]S. S. Iyer, R. A. Metzger, and F. G. Allen, J. Appl. Phys. **52**, 5608 (1982).

[10]P. R. Pukite, S. S. Iyer, and G. J. Scilla, Appl. Phys. Lett. **54**, 916 (1989).

[11]H. Sugiura, J. Appl. Phys. **51**, 2630 (1980).

[12]P. Fons, N. Hirashita, L. C. Markert, Y.-W. Kim, J. E. Greene, W.-X. Ni, J. Knall, G. V. Hansson, and J.-E. Sundgren, Appl. Phys. Lett. **53**, 1732 (1988).

[13]Y. Ota, J. Appl. Phys. **51**, 1102 (1980).

[14]M.-A. Hasan, J. Knall, S. A. Barnett, J.-E. Sundgren, L. C. Markert, A. Rockett, and J. E. Greene, J. Appl. Phys. **65**, 172 (1989).

[15]J.-P. Noel, N. Hirashita, L. C. Markert, Y.-W. Kim, J. E. Greene, J. Knall, W.-X. Ni, M.-A. Hasan, and J.-E. Sundgren, J. Appl. Phys. **65**, 1189 (1989).

[16]A. Rockett, S. A. Barnett, and J. E. Greene, J. Vac. Sci. Technol. B **2**, 306 (1984).

[17]M.-A. Hasan, J. Knall, S. A. Barnett, A. Rockett, J.-E. Sundgren, and J. E. Greene, J. Vac. Sci. Technol. B **5**, 1332 (1987).

[18]S. A. Barnett, H. F. Winters, and J. E. Greene, Surf. Sci. **165**, 303 (1986).

[19]Both the present experimental results and the work of Barnett *et al.* (Ref. 18) show no evidence for Sb_1^{2+} or Sb_3^{2+} ions. The likely presence of a small component of Sb_2^{2+} and Sb_4^{2+} at

Sb_1^+ and Sb_2^+ e/m positions, respectively, will have no effect on our results since we determined dopant ion fluxes from the measured ion current and the ion energy distribution using an average Sb ion cluster size (see text).

[20]G. Dearnaley, J. H. Freeman, and J. Stephen, *Ion Implantation* (North-Holland, Amsterdam, 1973); H. Kyssel and I. Ruge, *Ionenimplantation* (Teubner-Verlag, Stuttgart, 1978).
[21]R. N. Ghoshtagore, Phys. Rev. B **3**, 397 (1971).
[22]R. N. Ghoshtagore, Phys. Rev. B **3**, 2507 (1971).
[23]S. A. Barnett, H. F. Winters, and J. E. Greene, Surf. Sci. **181**, 596 (1987).
[24]S. Hofmann and J. Erlewein, Surf. Sci. **77**, 591 (1978).
[25]H. Jorke, Surf. Sci. **193**, 569 (1988).
[26]J. J. Harris, D. E. Ashenford, C. T. Foxon, P. J. Dobson, and B. A. Joyce, Appl. Phys. A **33**, 87 (1984).
[27]T. Sakamoto, N. J. Kawai, T. Nakagawa, K. Ohta, and T. Kojima, Appl. Phys. Lett. **47**, 617 (1985); S. A. Barnett and A. Rockett, Surf. Sci. **198**, 133 (1988).
[28]D. J. Chandi, Phys. Rev. Lett. **44**, 43 (1979).
[29]R. Biswas and D. R. Hamann, in *Proceedings of the Materials Research Society Symposium,* edited by J. Broughton, W. Krakow, and S. T. Pantelides (MRS, Pittsburgh, 1986), Vol. 63, p. 173.
[30]F. F. Abraham and I. P. Batra, Surf. Sci. **163**, 1752 (1985).
[31]See, for example, S. E. Koonin, *Computational Physics* (Benjamin/Cummings, Menlo Park, New Jersey, 1986).
[32]S. A. Barnett and J. E. Greene, Surf. Sci. **151**, 67 (1985).